ACS APPLIED MATERIALS & INTERFACES

www.acsami.org Research Article

Thermal Annealing-Induced Phase Conversion in N-type Triple-Cation Lead-Based Perovskite Field Effect Transistors

Taehyun Kong,[⊥] Yongjin Kim,[⊥] Jaeyoon Cho, Hyeonmin Choi, Youcheng Zhang, Heebeom Ahn, Jaeyong Woo, Dohyun Kim, Jeongjae Lee, Henning Sirringhaus, Takhee Lee,* and Keehoon Kang*

Cite This: *ACS Appl. Mater. Interfaces* 2025, 17, 8501−8512 Read Online

ACCESS | Metrics & More | Article Recommendations | Supporting Information

ABSTRACT: The field of perovskite optoelectronics and electronics has rapidly advanced, driven by excellent material properties and a diverse range of fabrication methods available. Among them, triple-cation perovskites such as $CsFAMAPbI_3$ offer enhanced stability and superior performance, making them ideal candidates for advanced applications. However, the multicomponent nature of these perovskites introduces complexity, particularly in how their structural, optical, and electrical properties are influenced by thermal annealing—a critical step for achieving high-quality thin films. Here, we propose a comprehensive mechanistic picture of the thin film formation process of $CsFAMAPbI_3$ during the thermal annealing step through systematic and comparative analyses, identifying two key thermally induced phase transitions: the crystallization of the perovskite phase facilitated by solvent evaporation and the formation of the PbI_2 phase due to thermal decomposition. Our results reveal that the crystallization process during annealing proceeds from the surface to the bulk of the films, with a significant impact on the film's morphology and optical characteristics. Controlled annealing enhances field-effect transistor device performance by promoting defect passivation and complete perovskite crystallization, while prolonged annealing leads to excessive PbI_2 formation, accelerating ion migration and ultimately degrading device performance. These insights offer valuable guidance for optimizing the design and performance of perovskite-based electronic and optoelectronic devices.

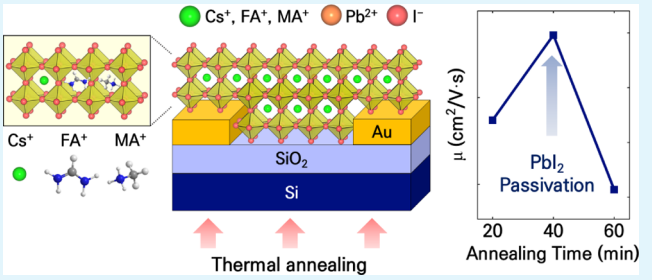

KEYWORDS: *perovskite, field effect transistor, thermal annealing, phase conversion, defect passivation*

INTRODUCTION

The field of perovskite optoelectronics and electronics, including applications such as solar cells,[1,2] light-emitting diodes,[3,4] photodetectors,[5,6] and field-effect transistors (FETs),[7,8] has experienced rapid growth due to its advantages owing to their unique material properties and versatile fabrication methods. Specifically, triple-cation perovskites, such as $CsFAMAPbI_3$, have attracted significant attention for their enhanced stability and superior performance across various applications.[9,10] The inclusion of the MA cation, known for its high dipole moment, in FA perovskites has improved structural stability by enhancing interactions with PbI_6 octahedra.[11] Furthermore, the addition of the Cs cation in these triple-cation perovskites further enhanced stability. This is primarily due to the small ion size of Cs, which effectively adjusts the Goldschmidt tolerance factor, leading to a more stable structure.[9]

Many of these perovskite-based devices require, however, the perovskite active material to be in the thin film form to allow efficient charge transport across the active layer. This condition thus necessitates the exploration of various methods for efficient thin film deposition and, more importantly, understanding of the exact mechanism behind thin film formation and growth in order to allow control of the film quality resulting from such deposition techniques.

In this aspect, spin-coating of solutions containing the halide precursors on a substrate, followed by antisolvent treatment and thermal annealing, has largely been the method of choice for fabricating perovskite thin films due to its simplicity and scalability.[12] However, despite a large number of studies on the influences of processing conditions (solvent, antisolvent, substrate, precursor, etc.) on the resulting films,[13−15] the exact process of perovskite film formation from precursors is still not completely understood with heavy reliance on empirical anecdotes.

Here, we wish to tackle this problem by focusing on the effect of the thermal annealing step following spin-coating on the resulting structural, optical, and transport properties of triple-cation perovskite thin films. Thermal annealing step is

Received: October 4, 2024
Revised: December 26, 2024
Accepted: December 26, 2024
Published: January 3, 2025

https://doi.org/10.1021/acsami.4c17017
ACS Appl. Mater. Interfaces 2025, 17, 8501−8512

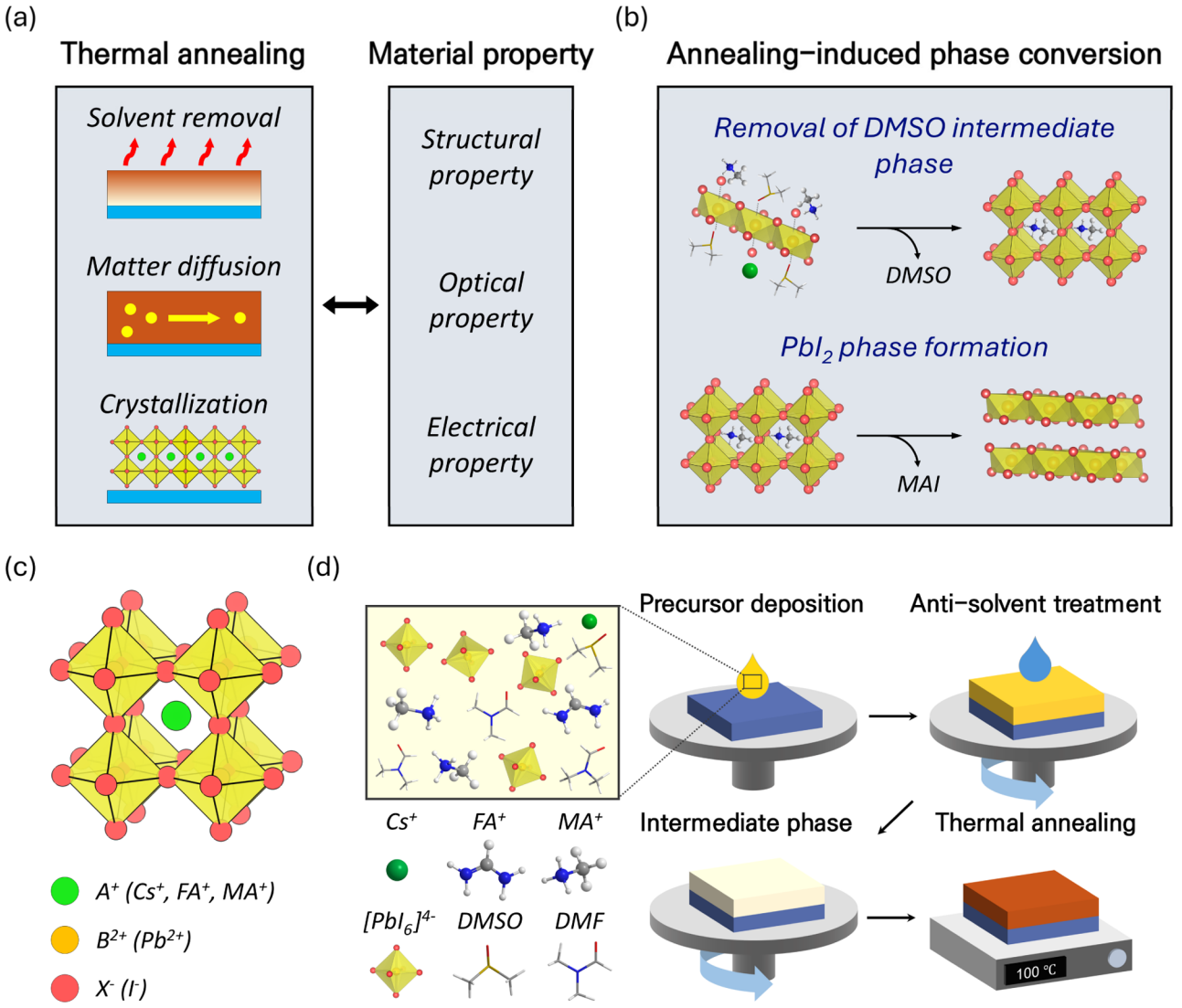

Figure 1. (a) Role of thermal annealing and related material properties. (b) Main phase conversion processes during thermal annealing. Schematics of (c) triple-cation perovskite structure and (d) film fabrication process.

crucial for removing of the residual solvent for perovskite precursors such as dimethylformamide (DMF) and dimethyl sulfoxide (DMSO), as well as for initiating supersaturation, a key process for nucleation and structural reorganization.[16,17] This transformation converts the spin-coated film from an amorphous or semicrystalline state into a favorable crystalline form with large grains.[18,19]

However, the structural changes induced by thermal annealing can also lead to nonuniformities within the thin films,[20,21] which are particularly problematic in the case of triple-cation perovskites. These materials, being multicomponent, are more susceptible to variations during the annealing process due to the different thermal sensitivities of the Cs, FA, and MA cations, as well as their varying interactions with solvents like DMF and DMSO during the spin-coating process.[22,23] Such nonuniformities pose significant challenges, as they can critically affect the optical and electronic properties of thin films. Therefore, a thorough understanding of the structural transformations during thermal annealing and how these changes affect the optical and electrical properties of the films is crucial for optimizing the performance of perovskite-based devices. By employing a comprehensive set of structural, optical, and electrical analyses, as illustrated in Figure 1a, this research provides an in-depth understanding of the film's structural evolution during annealing. These analyses also explore how the observed structural changes influence the performance of FET devices fabricated by using the annealed films.

The key idea of this research is to understand the dual impact of thermal annealing on the crystallization process of $CsFAMAPbI_3$ films (Figure 1b). First, annealing leads to the disappearance of intermediate phases, which is crucial in determining the crystallization direction and overall film structure.[24,25] Second, the thermal decomposition of organic cations results in the formation of PbI_2, which plays a significant role in passivation and charge transport within the films.[26,27] By elucidating these processes, the research not only enhances our understanding of perovskite thin film formation but also provides critical insights into how these structural changes affect the performance of devices such as FETs fabricated from these films. This research is driven by the need to clarify these processes, offering fundamental insights that can help optimize the performance of perovskite thin films in various practical applications.

https://doi.org/10.1021/acsami.4c17017
ACS Appl. Mater. Interfaces 2025, 17, 8501−8512

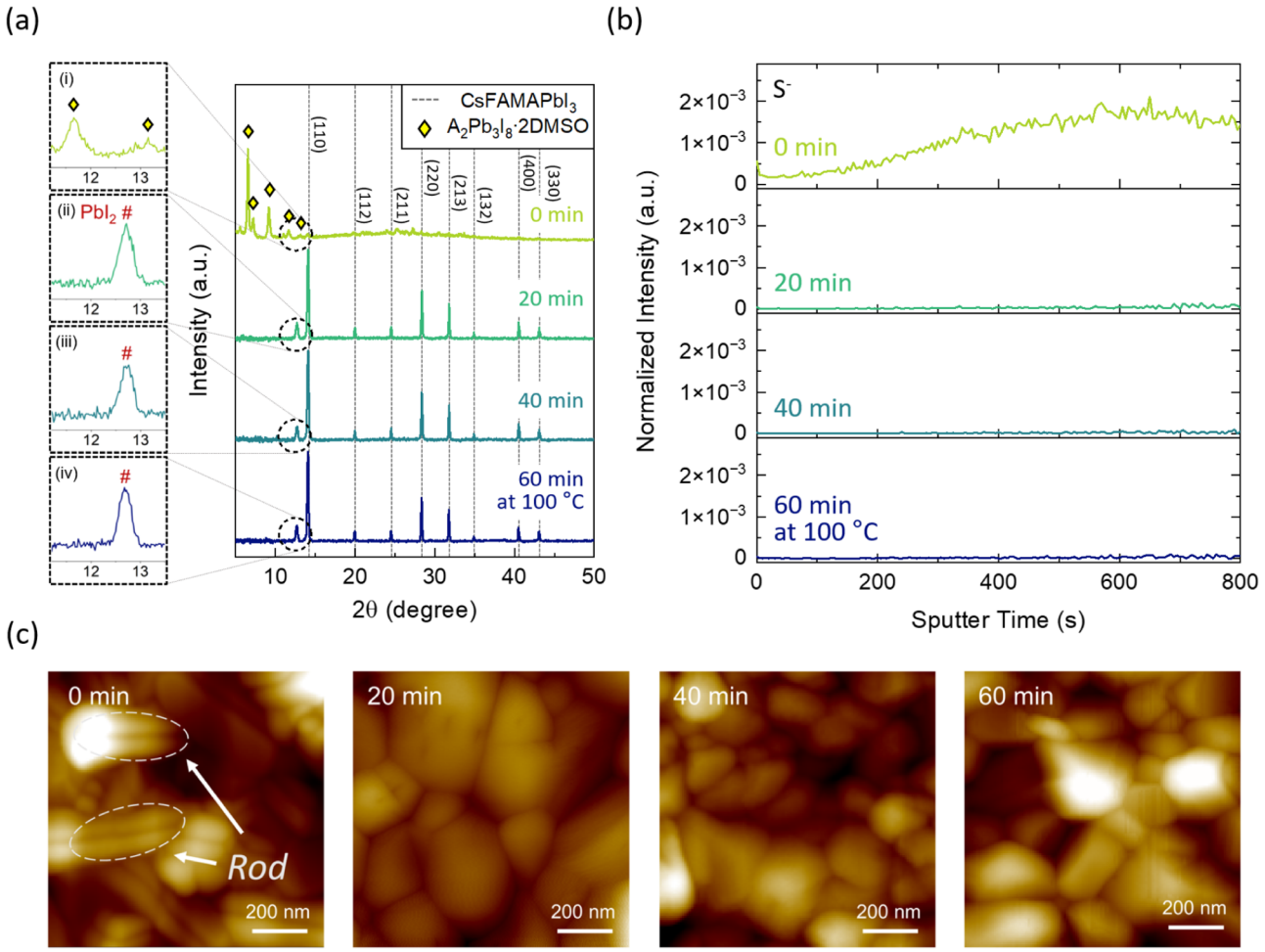

Figure 2. (a) XRD spectra, (b) time-of-flight secondary ion mass spectrometry (ToF-SIMS) depth profile of sulfide ion, and (c) AFM images for $CsFAMAPbI_3$ films with different annealing times.

RESULTS AND DISCUSSION

The perovskite films used in this study are triple-cation perovskite structures, where the A-site in the ABX_3 perovskite lattice is occupied by a mixture of Cs^+, MA^+ (methylammonium), and FA^+ (formamidinium) cations, the B-site is occupied by Pb^{2+} ions, and the X-site is filled with I^- ions, as illustrated in Figure 1c. The film fabrication process followed a widely adopted method in perovskite research,[28,29] involving the use of a solution containing DMF and DMSO solvents mixed with halide precursors, which was deposited onto a substrate. This was followed by spin coating, during which an antisolvent dropping process was employed to induce supersaturation.[30,31] Finally, the films underwent thermal annealing at 100 °C to achieve the desired crystallization (Figure 1d). Detailed information regarding the film preparation process can be found in the Supporting Information.

To investigate the overall structural changes in $CsFAMAPbI_3$ films induced by annealing, X-ray diffraction (XRD) measurements were conducted at various annealing times (Figure 2a). Initially, the as-cast film exhibited the $A_2Pb_3I_8$·2DMSO intermediate phase (referred to as the DMSO intermediate phase hereafter), characteristic of a one-dimensional structure within a hexagonal crystal system.[32] Previous studies have shown that both Cs and MA, which occupy the A-site, readily form the $A_2Pb_3I_8$·2DMSO intermediate phase,[24,33−35] while FA, also an A-site cation, is less likely to participate due to its lower Lewis acidity.[36] Our analysis suggests that this intermediate phase is primarily composed of MA, with minor contributions from Cs (details on the composition of the intermediate phase and the resultant vertical location of A-site cations in the film are provided in Figure S2 and Supporting Information Section 2.). As the annealing progressed, this intermediate phase gradually disappeared, revealing the transformation to the perovskite structure. Further annealing induces the formation of PbI_2 (see the inset in Figure 2a), which will be discussed in more details later. To further examine the film morphology, atomic force microscopy (AFM) was employed (Figure 2c). Consistent with the XRD results, the as-cast film displayed rod-like DMSO intermediate phases which were no longer present in the annealed samples.[37,38] These findings confirm that annealing eliminates the DMSO solvent, leading to a phase transformation from an intermediate phase to a perovskite structure.

ToF-SIMS depth profiling demonstrated the directional crystallization of the films during annealing, as shown in Figure 2b. Tracking S^- ions as indicators for the presence of DMSO,[39] we observed two distinct phenomena: First, the overall intensity of S^- signals diminished rapidly with increased annealing time, which reflects the evaporation of the residual DMSO molecules from the film. Second, the depth profiling

https://doi.org/10.1021/acsami.4c17017
ACS Appl. Mater. Interfaces 2025, 17, 8501−8512

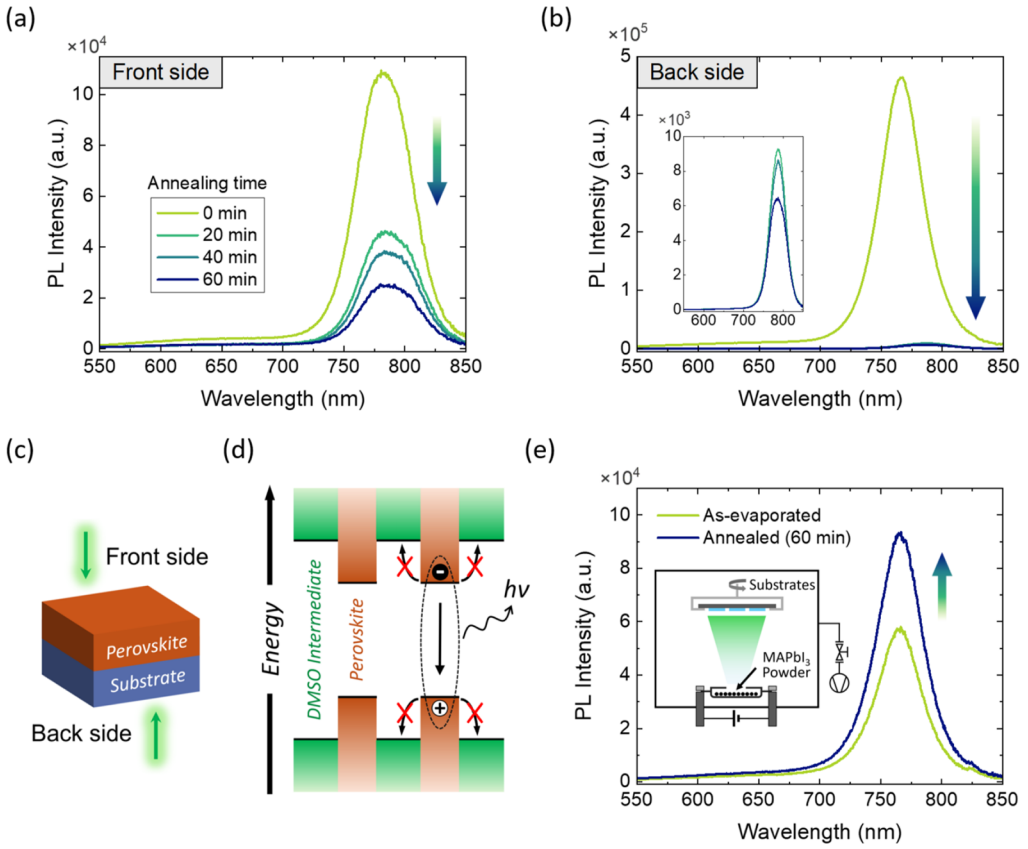

Figure 3. (a) Front side and (b) back side PL spectra of $CsFAMAPbI_3$ films deposited on glass with different annealing times under 450 nm excitation. (c) Schematic of the PL measurement configuration and (d) the suggested mechanism addressing high PL intensity of as-cast films (green: DMSO intermediate phase and brown: perovskite phase). (e) PL spectra of $MAPbI_3$ films deposited on glass by thermal evaporation before and after annealing under 450 nm excitation (inset: schematic representing experimental configuration of thermal evaporation of the perovskite).

analysis of the as-cast film revealed that the S^- concentration was notably higher in the bulk than in the surface region. These observations confirm that DMSO solvent molecules have evaporated from the surface during spin-coating, while the bulk retains the DMSO intermediate phase before the thermal annealing step. Although the DMSO intermediate phase is present at the surface, as indicated by the 0.5° grazing incidence XRD (GI XRD) spectrum in Figure S1a, which reflects the structural characteristics near the surface (as eq S1 and Figure S1b indicate), unlike in the XRD spectra in Figure 2a, the DMSO intermediate phase predominantly exists within the bulk of the film, as shown in Figure 2b. Collectively, these results suggest that the crystallization process, driven by solvent evaporation during annealing, proceeds from the top surface toward the bulk of the film, with the intermediate phase in the bulk ultimately converting to the perovskite phase.

The above findings can be corroborated with steady-state photoluminescence (PL) measurements of triple-cation perovskite films. As previously noted, the transformation from the DMSO intermediate phase to the perovskite phase occurs from the surface to the bulk of the films. To observe the effects of this transformation, measurements were carried out in two configurations (see Figure 3c): (1) one examining through the top surface of the perovskite layer (front PL) and (2) the bottom surface through the glass substrate (back PL).

The analysis of the PL intensity from films annealed for different durations revealed a significant trend. Figure 3a,b displays the front PL and back PL spectra, respectively, measured with 450 nm excitation. In as-cast films, incomplete perovskite crystal growth is evident, as shown by a slight blue shift in the PL peak in Figure 3a,b, likely due to size effects.[40−42] The high PL intensity of as-cast films can be attributed to the DMSO intermediate phase, which acts as a passivating agent by impeding the transfer of photogenerated charge carriers in crystal nuclei.[33] This phase forms a Type 1 heterojunction with the perovskite (Figure 3d), resulting in effective PL characteristics. Additionally, there is a clear reduction in the PL intensity with an increased annealing time, and this reduction is more pronounced in the back PL measurements, indicating that the annealing-induced crystallization process may differ between the surface and the bulk of the films. As observed in Figure 2b, this phenomenon can be attributed to the DMSO intermediate phase being more prevalent in the bulk than at the surface. Consequently, as this intermediate phase transforms into the perovskite phase, the passivation effect diminishes more significantly in the bulk, leading to a more pronounced reduction in the PL intensity in the back PL measurements. Notably, this passivation effect is further confirmed by the fact that the larger amount of the DMSO intermediate phase in the bulk initially causes the PL intensity of the as-cast film to be higher in the back PL measurement compared to the front PL measurement. The solvent effect can be supported further by our comparative annealing test between thermally evaporated and solution-processed perovskite films with a simpler yet analogous composition, $MAPbI_3$, which has been extensively studied and well-established in both thermal evaporation and solution-processing methods.[43,44] Unlike the solution-processed films

https://doi.org/10.1021/acsami.4c17017
ACS Appl. Mater. Interfaces 2025, 17, 8501−8512

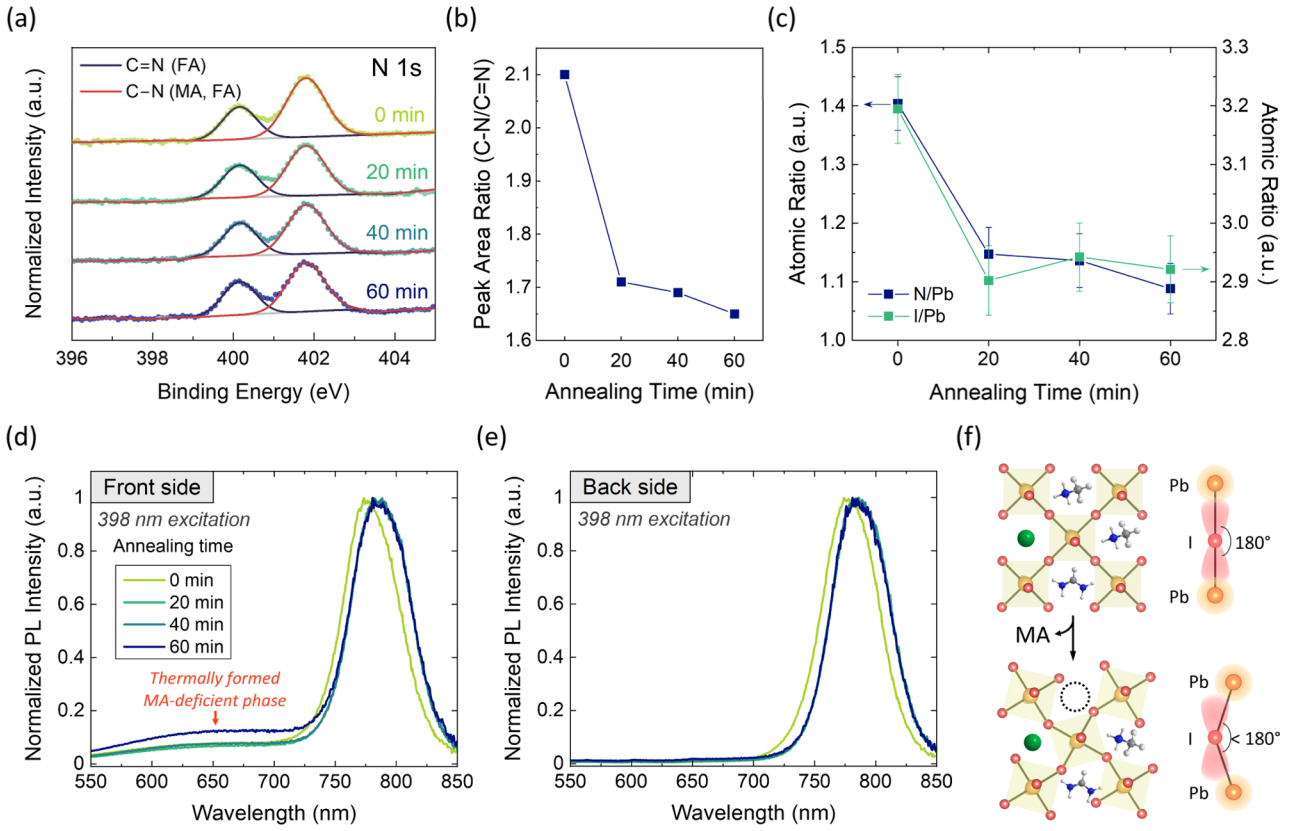

Figure 4. (a) N 1s XPS spectra and (b) ratio of integrated area under the peaks assigned to C═N (FA) and C−N (MA and FA) in the N 1s spectra of $CsFAMAPbI_3$ films with different annealing times. (c) Change in the N/Pb and I/Pb ratios of $CsFAMAPbI_3$ films with different annealing times. Normalized (d) front side and (e) back side PL spectra of $CsFAMAPbI_3$ films deposited on glass with different annealing times under 398 nm excitation. (f) Schematics representing structural evolution and the corresponding Pb−I−Pb angle before and after annealing.

(Figure S10), no reduction in PL intensity with annealing was observed in the thermally evaporated films (Figure 3e). This confirms that the reduction in PL intensity in the solution-processed perovskite films upon annealing is indeed due to the gradual conversion of the DMSO intermediate phase to the perovskite phase.

Considering our target stoichiometry of $Cs_{0.05}FA_{0.17}MA_{0.78}PbI_3$, any deviations from the stoichiometric ratio can be attributed to the formation of other phases induced by thermal annealing. As shown in Figure 2a, we anticipate the formation of the PbI_2 phase during the annealing process, which can be confirmed through compositional analysis via X-ray photoelectron spectroscopy (XPS) measurements. Specifically, the relative atomic ratios of nitrogen (N) and iodine (I) to lead (Pb) provide insights into the relative compositional shifts caused by thermal decomposition during the annealing of the triple-cation perovskite film, which may provide information toward the relative cation deficiency and the formation of different phases during the thermal annealing (Pb 4f and I 3d XPS spectra are included in Figure S3).

The N 1s XPS spectra in Figure 4a, with two distinct peaks centered at approximately 400.1 eV (C═N) and 401.8 eV (C−N), clearly indicate the coexistence of both FA and MA components.[22,27] The area ratios of these N 1s peaks after various annealing durations are presented in Figure 4b and detailed in Table S5 ($R^2 > 0.99$). A clear decreasing trend in the C−N/C═N ratio is observed in Figure 4b, which can be attributed to the thermal decomposition of MA (in the form of MAI) into CH_3I and NH_3, consistent with previously reported results.[22,27] This thermal decomposition of MA is further corroborated by the decreasing N/Pb ratio observed in Figure 4c. The decrease in the I/Pb ratio can also be linked to the thermal decomposition of MA, potentially leading to the formation of PbI_2 as MA decomposes, replacing the existing $CsFAMAPbI_3$ phase. Given the surface sensitivity of XPS, these elemental compositional changes suggest that annealing causes the surface to become deficient in MA while being relatively enriched in Pb.

Furthermore, front PL and back PL measurements were performed using a shorter excitation wavelength of 398 nm to examine more surface-sensitive optical properties during the thermal annealing influenced by PbI_2 formation due to the anticipated MA decomposition. A higher absorption coefficient at 398 nm excitation (unlike the 450 nm data shown in Figure 3a,b) results in a shallower optical penetration depth according to the Beer−Lambert law, thereby providing more surface-sensitive optical information, as calculated in Figure S4b,c, and Table S1 using absorbance data in Figures S4a and S5. The front PL spectrum exhibited a distinct broad emission peak between 600 and 700 nm (Figure 4d), which was absent in the back PL (Figure 4e). We propose that this broad peak arises from the phase transition at the interface between the PbI_2 phase formed from MA decomposition and the perovskite phase. Merdasa et al. reported a similar broad peak at 600 to 700 nm in films with a thermally evaporated PbI_2 layer on perovskite films, explaining that a reduced Pb−I−Pb angle in the MA-deficient transition phase decreases orbital overlap between Pb s orbitals and I p orbitals, resulting in an increase

https://doi.org/10.1021/acsami.4c17017
ACS Appl. Mater. Interfaces 2025, 17, 8501−8512

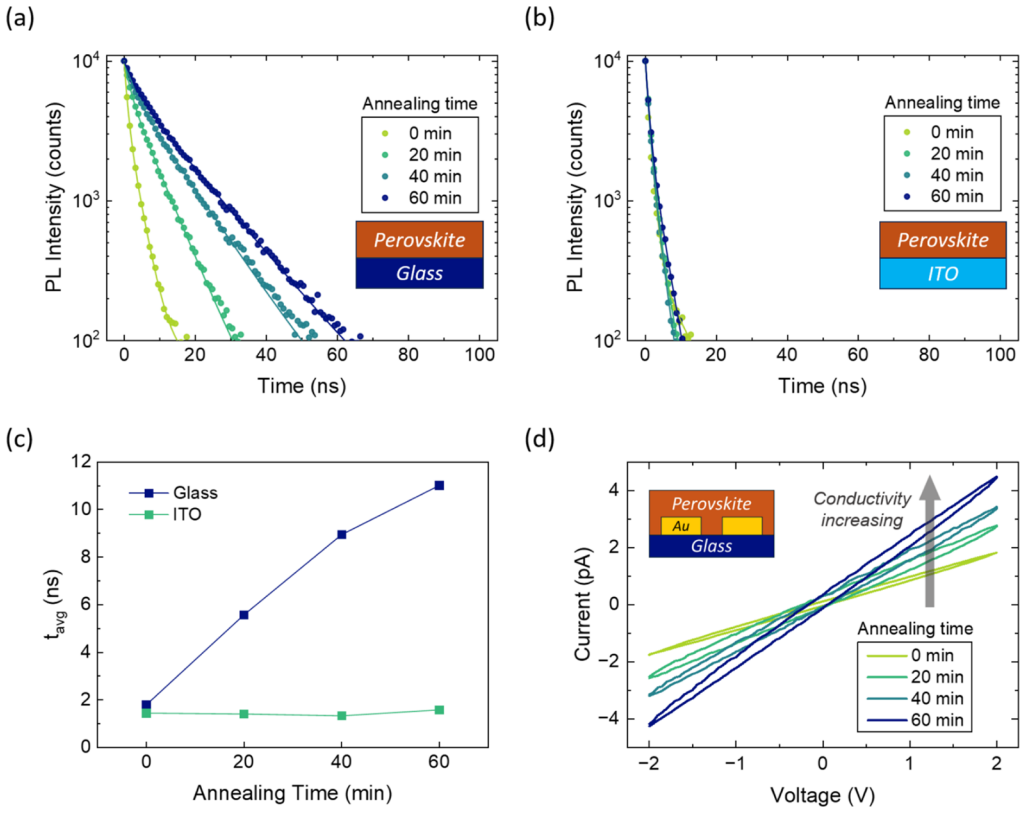

Figure 5. PL decay curves for $CsFAMAPbI_3$ films deposited on (a) glass and (b) ITO with different annealing times. (c) Average lifetimes extracted from PL decay curves. (d) $I-V$ curves for $CsFAMAPbI_3$ films with different annealing times (Inset: Experimental setup for the conductivity measurement, W: 1 mm, L: 0.2 mm).

in the bandgap, as depicted in Figure 4f.[45,46] Similarly, we suggest that this broad peak signifies the presence of an MA-deficient transition phase rather than being directly attributed to the PL of the PbI_2 phase itself.

The presence of the PbI_2 phase was also found to affect the transport properties of the $CsFAMAPbI_3$ film significantly, as can be seen from time-resolved photoluminescence (TRPL) and dark conductivity measurements. Figure 5a,b displays the TRPL spectra of perovskite films measured on glass (non-quenching) and indium tin oxide (ITO) (quenching) substrates, respectively, after various thermal annealing durations using an excitation wavelength of 405 nm. The TRPL data from the glass substrate, fitted using a biexponential function (see Table S2 for the fitting parameters), confirms that the PL lifetime (t_{avg}) increases with annealing time, which can be attributed to longer-lived photogenerated electron–hole pairs due to the defect passivation effect of the PbI_2 phase on the surface of the film.[47,48] For the triple-cation perovskite film on the ITO substrate (Figure 5b), the as-cast sample shows nearly the same PL lifetime as that of the glass substrate (Figure 5a). However, the PL lifetime of the annealed samples on the ITO substrate varies only slightly, primarily due to the quenching of the photogenerated electron–hole pairs at the interface with the underlying ITO layer,[49,50] which can be supported by the steady-state PL spectra in Figure S6b. The compiled trend of the PL lifetime according to the different annealing times is shown in Figure 5c, which quantitatively shows that t_{avg} monotonically increases for the glass samples from 1.789 ns (as-cast) to 11.01 ns (60 min annealed), whereas in ITO samples, t_{avg} slightly decreases until 40 min annealing, after which t_{avg} increases again for the 60 min annealing. This may show an interplay between 1) the reduced nonradiative recombination at the top interface and 2) enhanced charge transport toward the bottom interface (and therefore the greater degree of quenching by the ITO layer). Both can be resulted from the conversion from the intermediate to the perovskite phase, followed by the defect passivation by the PbI_2 phase formed during the annealing process. Furthermore, the above observation can be understood by the estimated optical penetration depth and carrier diffusion length that, when combined, eventually exceed the thickness of the perovskite film (Table S4), which confirms the extent of bulk transport of the photogenerated carriers all the way to the substrate (see Tables S2, S4, Figure S6, and eq S2 in Supporting Information Section 5). The enhanced transport can also be confirmed by the dark conductivity measurements (Figure 5d and Table S6) which show that the electrical conductivity increases with thermal annealing.

The effect of the thermal annealing can be highlighted by its impact on the performance of a FET device based on $CsFAMAPbI_3$ films prepared by various annealing times. The FET measurements were conducted on devices fabricated with a bottom-gate, bottom-contact (BGBC) structure, featuring a channel length of 200 μm and a channel width of 1 mm, using the same batch of devices annealed for different time durations in parallel. Interestingly, we found that the FET device annealed for 0 min did not function properly as shown in Figure 6a, indicating the absence of a fully formed perovskite phase or insufficient crystallization. This may be attributed to hindered charge transport caused by the residual DMSO intermediate phase located in proximity to the perovskite–dielectric interface. However, the device becomes functional as

https://doi.org/10.1021/acsami.4c17017
ACS Appl. Mater. Interfaces 2025, 17, 8501–8512

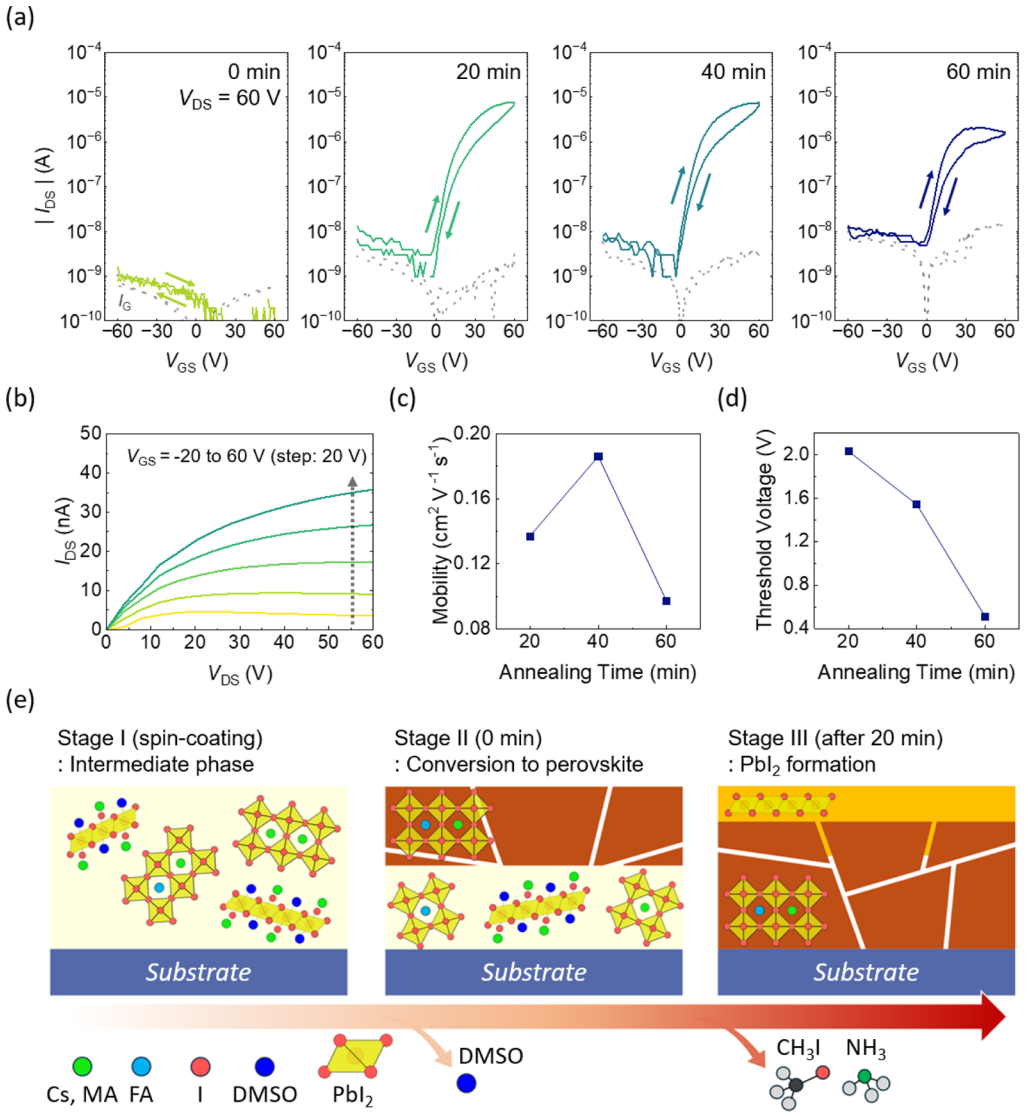

Figure 6. (a) Transfer characteristics of $CsFAMAPbI_3$ in the BGBC structure after different annealing times and (b) output characteristic of $CsFAMAPbI_3$ at different gate voltages after 40 min annealing. Extracted (c) mobility and (d) threshold voltage after different annealing times. (e) Schematics representing proposed overall mechanism under structural and compositional evolution during annealing.

an FET device after 20 min of annealing, with the mobility increasing until 40 min, before decreasing again for 60 min of annealing treatment (Figure 6c and Table S7).

The increase in mobility observed from 20 to 40 min of annealing can be attributed to the reduction in the concentration of defects and the grain growth during the conversion of the intermediate phase to perovskite phase facilitated by the annealing process, as well as the passivation effect of the PbI_2 phase. However, as the annealing time extended to 60 min, the mobility decreased, which is likely due to the excessive formation of the PbI_2 phase, which, while initially beneficial for passivation, eventually becomes detrimental to FET performance due to increased ion migration of the PbI_2 phase that can induce gate-field screening.[29,51−54]

The transfer curve of the FET device annealed for 40 min (Figure 6a) clearly shows an optimal device performance and therefore the optimal annealing time with the output curve (Figure 6b) showing an effective modulation of the channel conductance at various gate voltages. The output curves for the other annealing times are provided in Figure S7 for further comparison.

Additionally, the threshold voltage of the FET devices was observed to decrease progressively with increasing annealing time, as shown in Figure 6d. This trend can be related to the aforementioned deficiency of MA^+ and an enrichment of Pb^{2+} induced by thermal annealing (Figure 4) that can result in intrinsic n-type doping of the perovskite material.[55−58] This intrinsic doping is consistent with the reduction in the threshold voltage observed, as it shifts the Fermi level closer to the conduction band, making it easier to turn on the channel. These results corroborate the earlier findings from the $CsFAMAPbI_3$ films, showing that while thermal annealing improves device performance up to a certain extent, excessive annealing leads to adverse effects, likely due to the over-formation of the PbI_2 phase (i.e., relatively low mobility path) and the resultant ion migration. While the influence of changes in contact resistance due to annealing could be considered, they are unlikely to significantly contribute to the observed mobility decrease. A previous study on 3D Pb-based perovskite

https://doi.org/10.1021/acsami.4c17017
ACS Appl. Mater. Interfaces 2025, 17, 8501−8512

FETs[10] showed that contact resistance is more pronounced in devices with shorter channel lengths (~20 μm), whereas its impact becomes negligible for longer channels, such as the 200 μm devices employed in this work. Therefore, the reduction in mobility is more likely due to the excessive PbI_2 formation rather than contact resistance. Additionally, the conductivity measurement (Figure 5d) showed that the current did not decrease with prolonged thermal annealing, indicating that the contact resistance was not significantly affected by the annealing process. To validate our measurements, we also conducted FET measurements using a bottom-gate top-contact (BGTC) structure, which showed similar device characteristics to the BGBC structure and similar trends in the variations of both mobility and threshold voltage with thermal annealing (Figure S8). From this comparison, we note that the previously discussed thermal annealing effects on the structure and electrical transport properties of $CsFAMAPbI_3$ can be directly related to the observed FET device characteristics, irrespective of the device configuration. We note that there is a finite hysteresis in clockwise direction in our $CsFAMAPbI_3$ FET devices similarly to previous reports on perovskite FET devices.[59−63] Although beyond the scope of this work, we observe a smaller hysteresis in BGTC devices (see Table S8), which might be related to the different extent of interfacial polarization for bottom contact and top contact devices.[10,28,64−66]

The findings from this work can be mechanistically summarized, as shown in Figure 6e. In Stage I (spin-coating), we find that a significant fraction of the film exists as the $A_2Pb_3I_8{\cdot}2DMSO$ intermediate phase. The initial effect of thermal annealing (stage II) is the phase transformation to the desired perovskite phase, primarily driven by solvent (DMSO) evaporation, which occurs downward from the top surface. The effect of further thermal annealing (Stage III) is a complete conversion of the film to the $CsFAMAPbI_3$ perovskite phase, followed by the vaporization of MA^+ that induces the local PbI_2 formation at the top surface that can passivate defects in the film if present at the right optimal level. We expect that our findings can be further generalized to other solution-processed perovskite materials that contain MA^+ ions and DMSO solvent, including solution-processed $MAPbI_3$ perovskite for which the same trend can be observed (see Figures S9−S13 and Table S3 in Supporting Information Section 7).

CONCLUSIONS

Overall, this study aims to elucidate the role of thermal annealing in the film formation process of a representative spin-coated triple-cation perovskite $CsFAMAPbI_3$ film and its impact on FET device characteristics. A systematic and comprehensive analysis of the structural, optical, and transport properties of $CsFAMAPbI_3$ films treated by different annealing treatment durations highlights the structural and compositional evolution of the $CsFAMAPbI_3$ films. Our results demonstrate that annealing initiates the phase conversion of the DMSO intermediate phase to the desired perovskite phase driven by solvent evaporation. The optical and structural analyses reveal the downward crystallization from the top surface that gradually progresses toward the bulk. Importantly, this study highlights the intricate balance required during the annealing process; while moderate annealing enhances the film quality by reducing the number of defects and promoting grain growth, excessive annealing leads to over-formation of the PbI_2 phase, which can be detrimental to device performance. This effect is particularly evident in the FET devices, where field-effect mobility improvement was clearly observed with a moderate annealing treatment, owing to the defect passivation of the PbI_2 phase in addition to a complete crystallization of the perovskite phase. Our findings present an intricate interplay between thermally induced phase conversion, crystal growth, and decomposition effects that underscore the critical role of controlled thermal annealing treatment in optimizing the performance of $CsFAMAPbI_3$-based FET devices, which can be extended to provide insights for the future development of high-performance perovskite-based electronic and optoelectronic devices.

EXPERIMENTAL SECTION

Materials. Cesium iodide (CsI), Formamidinium iodide (FAI), Lead iodide (PbI_2), DMSO, DMF, and Chlorobenzene were all purchased from Sigma-Aldrich. Methylammonium iodide (MAI) was purchased from GreatCell Solar. All materials were stored in a nitrogen-filled glovebox and used as received without further purification.

Solvent-Based Perovskite Film Preparation. The triple-cation perovskite ($Cs_{0.05}FA_{0.17}MA_{0.78}PbI_3$) precursor solution with a concentration of 0.8 M was prepared by dissolving 0.12 mmol (31 mg) of CsI, 0.41 mmol (70 mg) of FAI, 1.87 mmol (298 mg) of MAI, and 2.4 mmol (1106 mg) of PbI_2 in a solution comprising 2.4 mL of DMF and 0.6 mL of DMSO. The triple-cation perovskite precursor solution with a concentration of 1.2 M was prepared by dissolving 0.18 mmol (47 mg) of CsI, 0.62 mmol (105 mg) of FAI, 2.81 mmol (447 mg) of MAI, and 3.6 mmol (1659 mg) of PbI_2 in a solution comprising 2.4 mL of DMF and 0.6 mL of DMSO.

For the $MAPbI_3$ perovskite precursor solution, 2.4 mmol (382 mg) of MAI and 2.4 mmol (1106 mg) of PbI_2 were dissolved in a solution containing 2.4 mL of DMF and 0.6 mL of DMSO.

All perovskite precursor solution mixtures were stirred overnight within a nitrogen-filled glovebox and filtered with a 0.45 μm poly(vinylidene difluoride) filter before use.

Substrates were cleaned by sonication in water, acetone, and 2-propanol for 15 min each. Prepared precursor solutions were spin-coated at 5000 rpm for 35 s, with chlorobenzene introduced at the 10th second as an antisolvent, followed by annealing at 100 °C for 0, 20, 40, or 60 min. Films for absorbance spectroscopy and AFM were prepared on glass substrates (Eagle XG, Corning), while films for XRD, GI-XRD, XPS, and ToF-SIMS were prepared on silicon substrates. For steady-state PL and TRPL measurements, films were prepared on both glass and ITO-coated glass substrates. (For TRPL measurements, 1.2 M precursor was used to fabricate 400 nm-thick perovskite films. Otherwise, every film fabrication used 0.8 M precursor solution). Prior to spin coating for conductivity measurements and BGBC FET fabrication, 4 nm Ti/40 nm Au electrodes were deposited on bare glass and SiO_2 substrate (300 nm SiO_2 on n^{++} silicon), respectively, by thermal evaporation. The pattern of the deposited electrodes is indicated in the inset of Figure 5d. For the BGTC FET fabrication, the Au electrodes were deposited after the spin coating of perovskite films. All prepared films were stored in a nitrogen-filled glovebox for 1 day before characterization.

Solvent-Free Perovskite Film Preparation. For the mechanochemical synthesis of $MAPbI_3$ powder used in thermal evaporation (Figure 3e), 3.6 mmol (572 mg) of MAI and 3.6 mmol (1660 mg) of PbI_2 were placed into an alumina jar with two balls, each 28.65 g and 1.9 cm in diameter. Subsequently, the jar was shaken by ball mill equipment (Retsch, Mixer Mill MM-400) at a frequency of 20 Hz for 90 min 1.05 mmol (650 mg) of synthesized $MAPbI_3$ powder and 0.52 mmol (83 mg) of MAI were loaded on a tungsten boat inside a vacuum chamber, 30 cm below the cleaned glass substrates. The tungsten boat was quickly heated by passing a current of 140 A through it for 2 min.

https://doi.org/10.1021/acsami.4c17017
ACS Appl. Mater. Interfaces 2025, 17, 8501−8512

Structural Characterizations. Normal mode XRD was performed using an X-ray diffractometer (Bruker, New D8 ADVANCE), and GI mode XRD was performed using an X-ray diffractometer (PANalytical, Xpert-Pro), both employing a Cu Kα radiation source with a wavelength of 1.5406 Å. The thickness and top-view surface profile of the perovskite films were characterized by an atomic force microscope (Park Systems, NX-10).

Compositional Characterizations. The vertical distribution of elements was analyzed by a time-of-flight secondary ion mass spectrometer (ION-TOF, TOF.SIMS 5) with a Bi^+ primary source (30 keV) and an Ar gas cluster (Ar_{1100}^+) ion source as the etching source (5 keV) at the National Center for Interuniversity Research Facilities (NCIRF) in Seoul National University. Depth profiles were normalized to total counts.[67] XPS was performed using an X-ray photoelectron spectrometer (Kratos Analytical, AXIS Supra) at the NCIRF.

Optical Characterizations. Steady-state PL measurements were conducted with a spectrofluorometer (JASCO, FP-8550) utilizing a Xe arc lamp with 398 and 450 nm excitation wavelengths. Measurement through the substrate side (Back PL) and perovskite side (Front PL) were both conducted as in Figure 3c. TRPL measurements were performed with a spectrophotometer (PicoQuant, FlouTime 300) with a 405 nm excitation wavelength. Carrier lifetimes were extracted by biexponential fitting using eq 1, in which $I(t)$, t_1, t_2, A_1, A_2, and B are the PL intensity at time t, decay time constants, corresponding decay amplitudes, and a constant.[68] Absorbance spectra were acquired by using a UV−vis spectrophotometer (JASCO, V-770).

$$I(t) = A_1 e^{-t/t_1} + A_2 e^{-t/t_2} + B \quad (1)$$

Electrical Characterizations. Conductivity measurements were conducted using a semiconductor parameter analyzer (HP Agilent, 4156B) in a vacuum environment (ca. 10^{-3} Torr), which can probe down to 1 fA. The current was measured as voltage double sweeps between −2 and 2 V at a sweep speed of 200 mV/s. Prior to the characterization of FETs, each device was prescratched, with a tip to minimize fringing effect and gate leakage.[69] The transfer characteristics of the FETs were examined by a semiconductor parameter analyzer (HP Agilent, 4155C) in the pulsed operation mode (with a pulse width of 1 ms and a pulse period of 1 s), while the output characteristics were measured under continuous operation mode. All FET measurements were held in a vacuum environment (ca. 10^{-6} Torr), following common methodologies in the field to exclude any damage and effects from degradation.[7,10,53,70] The saturation mobilities were calculated through eq 2, where L, W, C, I_{DS}, and V_{GS} are the channel length, channel width, areal dielectric capacitance, drain current, and gate voltage, respectively. The threshold voltages were extracted using linear fitting of $|\sqrt{I_{DS}}|$ with respect to V_{GS}.[71]

$$\mu = \frac{2L}{WC}\left(\frac{\partial\sqrt{I_{DS}}}{\partial V_{GS}}\right)^2 \quad (2)$$

ASSOCIATED CONTENT

Supporting Information

The Supporting Information is available free of charge at https://pubs.acs.org/doi/10.1021/acsami.4c17017.

GI mode XRD spectrum of an as-cast $CsFAMAPbI_3$ film and calculated X-ray penetration depths; ToF-SIMS depth profile of $CsFAMAPbI_3$ films; Pb 4f and I 3d XPS spectra of $CsFAMAPbI_3$ films; absorption spectra and calculated optical penetration depths of $CsFAMAPbI_3$ films; absorbance of $CsFAMAPbI_3$ films and a glass substrate; PL decay curves of 400 nm-thick $CsFAMAPbI_3$ films on ITO and PL spectra of 200 nm-thick $CsFAMAPbI_3$ films prepared on ITO substrates; fitting parameters of PL decay curves for $CsFAMAPbI_3$ films; output characteristics of $CsFAMAPbI_3$ in the BGBC structure; transfer characteristics of $CsFAMAPbI_3$ in the BGTC structure and extracted mobility and threshold voltage; XRD spectra of $MAPbI_3$ films; PL spectra of $MAPbI_3$ films; absorption spectra and calculated optical penetration depths of $MAPbI_3$ films; change in the N/Pb and I/Pb ratios of $MAPbI_3$ films; front PL spectra of thermally evaporated $MAPbI_3$ films under 398 nm excitation; thickness of $CsFAMAPbI_3$ films; ratio of integrated area under the peaks in the N 1s spectra of $CsFAMAPbI_3$ films; calculated conductivity of $CsFAMAPbI_3$ films; and evaluated mobility, threshold voltage, and hysteresis of $CsFAMAPbI_3$ (PDF)

AUTHOR INFORMATION

Corresponding Authors

Takhee Lee − *Department of Physics and Astronomy and Institute of Applied Physics, Seoul National University, Seoul 08826, Korea;* orcid.org/0000-0001-5988-5219; Email: tlee@snu.ac.kr

Keehoon Kang − *Department of Materials Science and Engineering, Research Institute of Advanced Materials, Seoul National University, Seoul 08826, Korea; Institute of Applied Physics, Seoul National University, Seoul 08826, Korea;* orcid.org/0000-0003-1230-3626; Email: keehoon.kang@snu.ac.kr

Authors

Taehyun Kong − *Department of Materials Science and Engineering, Research Institute of Advanced Materials, Seoul National University, Seoul 08826, Korea;* orcid.org/0009-0003-6936-6545

Yongjin Kim − *Department of Materials Science and Engineering, Research Institute of Advanced Materials, Seoul National University, Seoul 08826, Korea*

Jaeyoon Cho − *Department of Materials Science and Engineering, Research Institute of Advanced Materials, Seoul National University, Seoul 08826, Korea*

Hyeonmin Choi − *Department of Materials Science and Engineering, Research Institute of Advanced Materials, Seoul National University, Seoul 08826, Korea*

Youcheng Zhang − *Cavendish Laboratory, University of Cambridge, Cambridge CB3 0HE, U.K.*

Heebeom Ahn − *Department of Materials Science and Engineering, Research Institute of Advanced Materials, Seoul National University, Seoul 08826, Korea*

Jaeyong Woo − *Department of Physics and Astronomy, Seoul National University, Seoul 08826, Korea*

Dohyun Kim − *Department of Materials Science and Engineering, Research Institute of Advanced Materials, Seoul National University, Seoul 08826, Korea*

Jeongjae Lee − *Department of Materials Science and Engineering, Research Institute of Advanced Materials, Seoul National University, Seoul 08826, Korea;* orcid.org/0000-0003-4294-4993

Henning Sirringhaus − *Cavendish Laboratory, University of Cambridge, Cambridge CB3 0HE, U.K.;* orcid.org/0000-0001-9827-6061

Complete contact information is available at: https://pubs.acs.org/10.1021/acsami.4c17017

https://doi.org/10.1021/acsami.4c17017
ACS Appl. Mater. Interfaces 2025, 17, 8501−8512

Author Contributions

[⊥]T. Kong and Y. Kim contributed equally to this work.

Notes

The authors declare no competing financial interest.

■ ACKNOWLEDGMENTS

This work was supported by the Samsung Research Funding and Incubation Center of Samsung Electronics (under Project Number SRFC-MA2401-03), the National Research Foundation of Korea (NRF) grant (no. RS-2024-00342191 and no. 2021R1A2C3004783), the BrainLink Program (no. 2022H1D3A3A01077343), the Nano Material Technology Development Program grant (no. 2021M3H4A1A02049651) through NRF funded by the Ministry of Science and ICT of Korea, and the Korea Institute for Advancement of Technology(KIAT) grant funded by the Korea Government (Ministry of Education, P0025681-G02P22450002201-10054408, Semiconductor-Specialized University). K.K. appreciates support from the Creative-Pioneering Researchers Program through Seoul National University. Y.Z. and H.S. appreciate support from EPSRC programme grant (EP/W017091/1).

■ REFERENCES

(1) Park, J.; Kim, J.; Yun, H.-S.; Paik, M. J.; Noh, E.; Mun, H. J.; Kim, M. G.; Shin, T. J.; Seok, S. I. Controlled growth of perovskite layers with volatile alkylammonium chlorides. *Nature* **2023**, *616*, 724−730.

(2) Shen, Z.; Han, Q.; Luo, X.; Shen, Y.; Wang, Y.; Yuan, Y.; Zhang, Y.; Yang, Y.; Han, L. Efficient and stable perovskite solar cells with regulated depletion region. *Nat. Photonics* **2024**, *18*, 450−457.

(3) Gao, Y.; Li, H.; Dai, X.; Ying, X.; Liu, Z.; Qin, J.; Guo, J.; Han, Z.; Zhang, Y.; Zhu, M.; Wu, X.; Cai, Q.; Yang, Y.; Feng, L.; Zhang, X.; Huang, J.; He, H.; Gao, F.; Ye, Z. Microsecond-response perovskite light-emitting diodes for active-matrix displays. *Nat. Electron.* **2024**, *7*, 487−496.

(4) Li, X.; Lou, B.; Chen, X.; Wang, M.; Jiang, H.; Lin, S.; Ma, Z.; Jia, M.; Han, Y.; Tian, Y.; Wu, D.; Xu, W.; Li, X.; Ma, C.; Shi, Z. Deep-blue narrow-band emissive cesium europium bromide perovskite nanocrystals with record high emission efficiency for wide-color-gamut backlight displays. *Mater. Horiz.* **2024**, *11*, 1294−1304.

(5) Min, L.; Sun, H.; Guo, L.; Wang, M.; Cao, F.; Zhong, J.; Li, L. Frequency-selective perovskite photodetector for anti-interference optical communications. *Nat. Commun.* **2024**, *15*, 2066.

(6) Tang, Y.; Jin, P.; Wang, Y.; Li, D.; Chen, Y.; Ran, P.; Fan, W.; Liang, K.; Ren, H.; Xu, X.; Wang, R.; Yang, Y.; Zhu, B. Enabling low-drift flexible perovskite photodetectors by electrical modulation for wearable health monitoring and weak light imaging. *Nat. Commun.* **2023**, *14*, 4961.

(7) Bukke, R. N.; Syzgantseva, O. A.; A Syzgantseva, M.; Aidinis, K.; Soultati, A.; Verykios, A.; Tountas, M.; Psycharis, V.; Alshahrani, T.; Ullah, H.; P Zorba, L.; C Vougioukalakis, G.; Wang, J.; Bao, X.; Jang, J.; Nazeeruddin, M. K.; Vasilopoulou, M.; Mohd Yusoff, A. R. b.; Yusoff, A. R. Strain relaxation and multidentate anchoring in n-type perovskite transistors and logic circuits. *Nat. Electron.* **2024**, *7*, 444−453.

(8) Kim, Y.; Woo, J.; Jung, Y.-K.; Ahn, H.; Kim, I.; Reo, Y.; Lim, H.; Lee, C.; Lee, J.; Kim, Y.; Choi, H.; Lee, M.-H.; Lee, J.; Stranks, S. D.; Sirringhaus, H.; Noh, Y.-Y.; Kang, K.; Lee, T. Reversible oxidative p-doping in 2d tin halide perovskite field-effect transistors. *ACS Energy Lett.* **2024**, *9* (4), 1725−1734.

(9) Saliba, M.; Matsui, T.; Seo, J.-Y.; Domanski, K.; Correa-Baena, J.-P.; Nazeeruddin, M. K.; Zakeeruddin, S. M.; Tress, W.; Abate, A.; Hagfeldt, A.; Grätzel, M. Cesium-containing triple cation perovskite solar cells: improved stability, reproducibility and high efficiency. *Energy Environ. Sci.* **2016**, *9*, 1989−1997.

(10) Senanayak, S. P.; Abdi-Jalebi, M.; Kamboj, V. S.; Carey, R.; Shivanna, R.; Tian, T.; Schweicher, G.; Wang, J.; Giesbrecht, N.; Di Nuzzo, D.; Beere, H. E.; Docampo, P.; Ritchie, D. A.; Fairen-Jimenez, D.; Friend, R. H.; Sirringhaus, H. A general approach for hysteresis-free, operationally stable metal halide perovskite field-effect transistors. *Sci. Adv.* **2020**, *6* (15), No. eaaz4948.

(11) Binek, A.; Hanusch, F. C.; Docampo, P.; Bein, T. Stabilization of the trigonal high-temperature phase of formamidinium lead iodide. *J. Phys. Chem. Lett.* **2015**, *6* (7), 1249−1253.

(12) Park, N.-G.; Zhu, K. Scalable fabrication and coating methods for perovskite solar cells and solar modules. *Nat. Rev. Mater.* **2020**, *5*, 333−350.

(13) Taylor, A. D.; Sun, Q.; Goetz, K. P.; An, Q.; Schramm, T.; Hofstetter, Y.; Litterst, M.; Paulus, F.; Vaynzof, Y. A general approach to high-efficiency perovskite solar cells by any antisolvent. *Nat. Commun.* **2021**, *12*, 1878.

(14) Min, H.; Hu, J.; Xu, Z.; Liu, T.; Khan, S.-U.-Z.; Roh, K.; Loo, Y.-L.; Rand, B. P. Hot-casting-assisted liquid additive engineering for efficient and stable perovskite solar cells. *Adv. Mater.* **2022**, *34* (36), 2205309.

(15) Zhu, H.; Liu, A.; Kim, H.; Hong, J.; Go, J.-Y.; Noh, Y.-Y. High-performance layered perovskite transistors and phototransistors by binary solvent engineering. *Chem. Mater.* **2021**, *33* (4), 1174−1181.

(16) Lee, J. W.; Yu, H.; Lee, K.; Bae, S.; Kim, J.; Han, G. R.; Hwang, D.; Kim, S. K.; Jang, J. Highly crystalline perovskite-based photovoltaics via two-dimensional liquid cage annealing strategy. *J. Am. Chem. Soc.* **2019**, *141* (14), 5808−5814.

(17) Liu, H.; Liu, H.; Yang, J.; Yang, F.; Liu, Z.; Jain, S. M. Improving the performance of planar perovskite solar cells through a preheated, delayed annealing process to control nucleation and phase transition of perovskite films. *Cryst. Growth Des.* **2019**, *19* (8), 4314−4323.

(18) Yu, J. C.; Kim, D. W.; Kim, D. B.; Jung, E. D.; Park, J. H.; Lee, A.-Y.; Lee, B. R.; Di Nuzzo, D.; Friend, R. H.; Song, M. H. Improving the stability and performance of perovskite light-emitting diodes by thermal annealing treatment. *Adv. Mater.* **2016**, *28* (32), 6906−6913.

(19) Su, T.; Li, X.; Zhang, Y.; Zhang, F.; Sheng, Z. Temperature-modulated crystal growth and performance for highly reproducible and efficient perovskite solar cells. *Phys. Chem. Chem. Phys.* **2017**, *19*, 13147−13152.

(20) Kim, N.-K.; Min, Y. H.; Noh, S.; Cho, E.; Jeong, G.; Joo, M.; Ahn, S.-W.; Lee, J. S.; Kim, S.; Ihm, K.; Ahn, H.; Kang, Y.; Lee, H.-S.; Kim, D. Investigation of thermally induced degradation in CH3NH3PbI3 perovskite solar cells using in-situ synchrotron radiation analysis. *Sci. Rep.* **2017**, *7*, 4645.

(21) Zheng, D.; Raffin, F.; Volovitch, P.; Pauporté, T. Control of perovskite film crystallization and growth direction to target homogeneous monolithic structures. *Nat. Commun.* **2022**, *13*, 6655.

(22) Akbulatov, A. F.; Martynenko, V. M.; Frolova, L. A.; Dremova, N. N.; Zhidkov, I.; Tsarev, S. A.; Luchkin, S. Y.; Kurmaev, E. Z.; Aldoshin, S. M.; Stevenson, K. J.; Troshin, P. A. Intrinsic thermal decomposition pathways of lead halide perovskites APbX3. *Sol. Energy Mater. Sol. Cells* **2020**, *213*, 110559.

(23) Singh, M.; Abdelsamie, M.; Li, Q.; Kodalle, T.; Lee, D.-K.; Arnold, S.; Ceratti, D. R.; Slack, J. L.; Schwartz, C. P.; Brabec, C. J.; Tao, S.; Sutter-Fella, C. M. Effect of the precursor chemistry on the crystallization of triple cation mixed halide perovskites. *Chem. Mater.* **2023**, *35* (18), 7450−7459.

(24) Ahn, N.; Son, D.-Y.; Jang, I.-H.; Kang, S. M.; Choi, M.; Park, N.-G. Highly reproducible perovskite solar cells with average efficiency of 18.3% and best efficiency of 19.7% fabricated via Lewis base adduct of lead(II) iodide. *J. Am. Chem. Soc.* **2015**, *137* (27), 8696−8699.

(25) McMeekin, D. P.; Holzhey, P.; Fürer, S. O.; Harvey, S. P.; Schelhas, L. T.; Ball, J. M.; Mahesh, S.; Seo, S.; Hawkins, N.; Lu, J.; Johnston, M. B.; Berry, J. J.; Bach, U.; Snaith, H. J. Intermediate-phase engineering via dimethylammonium cation additive for stable perovskite solar cells. *Nat. Mater.* **2023**, *22*, 73−83.

https://doi.org/10.1021/acsami.4c17017
ACS Appl. Mater. Interfaces 2025, 17, 8501−8512

(26) Shan, D.; Tong, G.; Cao, Y.; Tang, M.; Xu, J.; Yu, L.; Chen, K. The effect of decomposed PbI2 on microscopic mechanisms of scattering in CH3NH3PbI3 films. *Nanoscale Res. Lett.* **2019**, *14*, 208.
(27) Zhidkov, I. S.; Boukhvalov, D. W.; Akbulatov, A. F.; Frolova, L. A.; Finkelstein, L. D.; Kukharenko, A. I.; Cholakh, S. O.; Chueh, C.-C.; Troshin, P. A.; Kurmaev, E. Z. XPS spectra as a tool for studying photochemical and thermal degradation in APbX3 hybrid halide perovskites. *Nano Energy* **2021**, *79*, 105421.
(28) Senanayak, S. P.; Dey, K.; Shivanna, R.; Li, W.; Ghosh, D.; Zhang, Y.; Roose, B.; Zelewski, S. J.; Andaji-Garmaroudi, Z.; Wood, W.; Tiwale, N.; MacManus-Driscoll, J. L.; Friend, R. H.; Stranks, S. D.; Sirringhaus, H. Charge transport in mixed metal halide perovskite semiconductors. *Nat. Mater.* **2023**, *22*, 216−224.
(29) Wang, S.; Kalyanasundaram, S.; Gao, L.; Ling, Z.; Zhou, Z.; Bonn, M.; Blom, P. W. M.; Wang, H. I.; Pisula, W.; Marszalek, T. Unveiling the role of linear alkyl organic cations in 2D layered tin halide perovskite field-effect transistors. *Mater. Horiz.* **2024**, *11*, 1177−1187.
(30) Zhang, F.; Shi, W.; Luo, J.; Pellet, N.; Yi, C.; Li, X.; Zhao, X.; Dennis, T. J. S.; Li, X.; Wang, S.; Xiao, Y.; Zakeeruddin, S. M.; Bi, D.; Grätzel, M. Isomer-pure bis-PCBM-assisted crystal engineering of perovskite solar cells showing excellent efficiency and stability. *Adv. Mater.* **2017**, *29* (17), 1606806.
(31) Bautista-Quijano, J. R.; Telschow, O.; Paulus, F.; Vaynzof, Y. Solvent−antisolvent interactions in metal halide perovskites. *Chem. Commun.* **2023**, *59*, 10588−10603.
(32) Rong, Y.; Tang, Z.; Zhao, Y.; Zhong, X.; Venkatesan, S.; Graham, H.; Patton, M.; Jing, Y.; Guloy, A. M.; Yao, Y. Solvent engineering towards controlled grain growth in perovskite planar heterojunction solar cells. *Nanoscale* **2015**, *7*, 10595−10599.
(33) Tian, L.; Zhang, W.; Huang, Y.; Wen, F.; Yu, H.; Li, Y.; Wang, Q.; Peng, C.; Ma, Z.; Hu, T.; Du, L.; Zhang, M. Effects of annealing time on triple cation perovskite films and their solar cells. *ACS Appl. Mater. Interfaces* **2020**, *12* (26), 29344−29356.
(34) Zai, H.; Zhang, D.; Li, L.; Zhu, C.; Ma, S.; Zhao, Y.; Zhao, Z.; Chen, C.; Zhou, H.; Li, Y.; Chen, Q. Low-temperature-processed inorganic perovskite solar cells via solvent engineering with enhanced mass transport. *J. Mater. Chem. A* **2018**, *6*, 23602−23609.
(35) Zhang, S.; Wu, S.; Chen, W.; Zhu, H.; Xiong, Z.; Yang, Z.; Chen, C.; Chen, R.; Han, L.; Chen, W. Solvent engineering for efficient inverted perovskite solar cells based on inorganic CsPbI2Br light absorber. *Mater. Today Energy* **2018**, *8*, 125−133.
(36) Lee, J.-W.; Dai, Z.; Lee, C.; Lee, H. M.; Han, T.-H.; De Marco, N.; Lin, O.; Choi, C. S.; Dunn, B.; Koh, J.; Di Carlo, D.; Ko, J. H.; Maynard, H. D.; Yang, Y. Tuning molecular interactions for highly reproducible and efficient formamidinium perovskite solar cells via adduct approach. *J. Am. Chem. Soc.* **2018**, *140* (20), 6317−6324.
(37) Guo, Y.; Shoyama, K.; Sato, W.; Matsuo, Y.; Inoue, K.; Harano, K.; Liu, C.; Tanaka, H.; Nakamura, E. Chemical pathways connecting lead (II) iodide and perovskite via polymeric plumbate (II) fiber. *J. Am. Chem. Soc.* **2015**, *137* (50), 15907−15914.
(38) Zhang, K.; Wang, Z.; Wang, G.; Wang, J.; Li, Y.; Qian, W.; Zheng, S.; Xiao, S.; Yang, S. A prenucleation strategy for ambient fabrication of perovskite solar cells with high device performance uniformity. *Nat. Commun.* **2020**, *11*, 1006.
(39) Xiao, S.; Bai, Y.; Meng, X.; Zhang, T.; Chen, H.; Zheng, X.; Hu, C.; Qu, Y.; Yang, S. Unveiling a key intermediate in solvent vapor postannealing to enlarge crystalline domains of organometal halide perovskite films. *Adv. Funct. Mater.* **2017**, *27* (12), 1604944.
(40) Ummadisingu, A.; Meloni, S.; Mattoni, A.; Tress, W.; Grätzel, M. Crystal-size-induced band gap tuning in perovskite films. *Angew. Chem., Int. Ed.* **2021**, *60* (39), 21368−21376.
(41) Zhang, H.; Wang, B.; Niu, Z.; Chen, G.; Guan, B.; Li, J.; Yu, J. Ultrasmall water-stable CsPbBr3 quantum dots with high intensity blue emission enabled by zeolite confinement engineering. *Mater. Horiz.* **2023**, *10*, 5079−5086.
(42) Droseros, N.; Longo, G.; Brauer, J. C.; Sessolo, M.; Bolink, H. J.; Banerji, N. Origin of the enhanced photoluminescence quantum yield in MAPbBr3 perovskite with reduced crystal size. *ACS Energy Lett.* **2018**, *3* (6), 1458−1466.
(43) Lee, J.; Lee, W.; Lee, J.; Baek, K.-Y.; Shin, J.; Kim, J.-K.; Kim, J.; Ahn, H.; Kang, K.; Lee, T. Tailored design-of-experiments approach for device performance prediction and optimization of flash-evaporated organic−inorganic halide perovskite-based photodetectors. *Adv. Mater. Technol.* **2021**, *6* (5), 2001131.
(44) Lee, W.; Lee, J.; Lee, H.-D.; Kim, J.; Ahn, H.; Kim, Y.; Yoo, D.; Lee, J.; Lee, T.-W.; Kang, K.; Lee, T. Controllable deposition of organic metal halide perovskite films with wafer-scale uniformity by single source flash evaporation. *Sci. Rep.* **2020**, *10*, 18781.
(45) Merdasa, A.; Kiligaridis, A.; Rehermann, C.; Abdi-Jalebi, M.; Stöber, J.; Louis, B.; Gerhard, M.; Stranks, S. D.; Unger, E. L.; Scheblykin, I. G. Impact of excess lead iodide on the recombination kinetics in metal halide perovskites. *ACS Energy Lett.* **2019**, *4* (6), 1370−1378.
(46) Merdasa, A.; Bag, M.; Tian, Y.; Källman, E.; Dobrovolsky, A.; Scheblykin, I. G. Super-resolution luminescence microspectroscopy reveals the mechanism of photoinduced degradation in CH3NH3PbI3 perovskite nanocrystals. *J. Phys. Chem. C* **2016**, *120* (19), 10711−10719.
(47) Chen, Q.; Zhou, H.; Song, T.-B.; Luo, S.; Hong, Z.; Duan, H.-S.; Dou, L.; Liu, Y.; Yang, Y. Controllable self-induced passivation of hybrid lead iodide perovskites toward high performance solar cells. *Nano Lett.* **2014**, *14* (7), 4158−4163.
(48) Park, B.-w.; Kedem, N.; Kulbak, M.; Lee, D. Y.; Yang, W. S.; Jeon, N. J.; Seo, J.; Kim, G.; Kim, K. J.; Shin, T. J.; Hodes, G.; Cahen, D.; Seok, S. I. Understanding how excess lead iodide precursor improves halide perovskite solar cell performance. *Nat. Commun.* **2018**, *9*, 3301.
(49) van Franeker, J. J.; Hendriks, K. H.; Bruijnaers, B. J.; Verhoeven, M. W. G. M.; Wienk, M. M.; Janssen, R. A. J. Monitoring thermal annealing of perovskite solar cells with in situ photoluminescence. *Adv. Energy Mater.* **2017**, *7* (7), 1601822.
(50) Stranks, S. D.; Eperon, G. E.; Grancini, G.; Menelaou, C.; Alcocer, M. J. P.; Leijtens, T.; Herz, L. M.; Petrozza, A.; Snaith, H. J. Electron-hole diffusion lengths exceeding 1 micrometer in an organometal trihalide perovskite absorber. *Science* **2013**, *342* (6156), 341−344.
(51) Jiang, Q.; Chu, Z.; Wang, P.; Yang, X.; Liu, H.; Wang, Y.; Yin, Z.; Wu, J.; Zhang, X.; You, J. Planar-structure perovskite solar cells with efficiency beyond 21. *Adv. Mater.* **2017**, *29* (46), 1703852.
(52) Jacobsson, T. J.; Correa-Baena, J.-P.; Halvani Anaraki, E.; Philippe, B.; Stranks, S. D.; Bouduban, M. E. F.; Tress, W.; Schenk, K.; Teuscher, J.; Moser, J.-E.; Rensmo, H.; Hagfeldt, A. Unreacted PbI2 as a double-edged sword for enhancing the performance of perovskite solar cells. *J. Am. Chem. Soc.* **2016**, *138* (32), 10331−10343.
(53) She, X.-J.; Chen, C.; Divitini, G.; Zhao, B.; Li, Y.; Wang, J.; Orri, J. F.; Cui, L.; Xu, W.; Peng, J.; Wang, S.; Sadhanala, A.; Sirringhaus, H. A solvent-based surface cleaning and passivation technique for suppressing ionic defects in high-mobility perovskite field-effect transistors. *Nat. Electron.* **2020**, *3*, 694−703.
(54) Wang, S.; Frisch, S.; Zhang, H.; Yildiz, O.; Mandal, M.; Ugur, N.; Jeong, B.; Ramanan, C.; Andrienko, D.; Wang, H. I.; Bonn, M.; Blom, P. W. M.; Kivala, M.; Pisula, W.; Marszalek, T. Grain engineering for improved charge carrier transport in two-dimensional lead-free perovskite field-effect transistors. *Mater. Horiz.* **2022**, *9*, 2633−2643.
(55) Euvrard, J.; Yan, Y.; Mitzi, D. B. Electrical doping in halide perovskites. *Nat. Rev. Mater.* **2021**, *6*, 531−549.
(56) Kim, Y.; Choi, H.; Lee, J.; Jung, Y.-K.; Jung, J.; Cho, J.; Lee, T.; Kang, K. Unlocking the potential of metal halide perovskite thermoelectrics through electrical doping: A critical review. *Ecomat* **2023**, *5* (11), No. e12406.
(57) Cao, K.; Zhu, J.; Wu, Y.; Ge, M.; Zhu, Y.; Qian, J.; Wang, Y.; Hu, K.; Lu, J.; Shen, W.; Liu, L.; Chen, S. Suppressing excess lead iodide aggregation and reducing n-type doping at perovskite/HTL

interface for efficient perovskite solar cells. *Small* **2023**, *19* (43), 2301822.
(58) Wang, X.; Liu, D.; Liu, R.; Du, X.; Zhang, B.; Sun, X.; Chen, C.; Li, Z.; Zhao, Q.; Shao, Z.; Wang, X.; Cui, G.; Pang, S. PbI6 octahedra stabilization strategy based on π-π stacking small molecule toward highly efficient and stable perovskite solar cells. *Adv. Energy Mater.* **2023**, *13* (11), 2203635.
(59) Cho, J.-H.; Go, J.-Y.; Bui, T. T.; Mun, S.; Kim, Y.; Ahn, K.; Noh, Y.-Y.; Kim, M.-G. Anion-vacancy-defect passivation of a 2d-layered tin-based perovskite thin-film transistor with sulfur doping. *Adv. Electron. Mater.* **2023**, *9* (3), 2201014.
(60) Zhang, Y.; Ummadisingu, A.; Shivanna, R.; Tjhe, D. H. L.; Un, H.-l.; Xiao, M.; Friend, R. H.; Senanayak, S. P.; Sirringhaus, H. Direct observation of contact reaction induced ion migration and its effect on non-ideal charge transport in lead triiodide perovskite field-effect transistors. *Small* **2023**, *19* (41), 2302494.
(61) Senanayak, S. P.; Yang, B.; Thomas, T. H.; Giesbrecht, N.; Huang, W.; Gann, E.; Nair, B.; Goedel, K.; Guha, S.; Moya, X.; Mcneill, C. R.; Docampo, P.; Sadhanala, A.; Friend, R. H.; Sirringhaus, H. Understanding charge transport in lead iodide perovskite thin-film field-effect transistors. *Sci. Adv.* **2017**, *3* (1), No. e1601935.
(62) Jeong, B.; Gkoupidenis, P.; Asadi, K. Solution-processed perovskite field-effect transistor artificial synapses. *Adv. Mater.* **2021**, *33* (52), 2104034.
(63) Xia, J.; Qiu, X.; Liu, Y.; Chen, P.-A.; Guo, J.; Wei, H.; Ding, J.; Xie, H.; Lv, Y.; Li, F.; Li, W.; Liao, L.; Hu, Y. Ferroelectric wide-bandgap metal halide perovskite field-effect transistors: toward transparent electronics. *Adv. Sci.* **2023**, *10* (10), 2300133.
(64) Yang, T.-Y.; Gregori, G.; Pellet, N.; Grätzel, M.; Maier, J. The significance of ion conduction in a hybrid organic-inorganic lead-iodide-based perovskite photosensitizer. *Angew. Chem., Int. Ed.* **2015**, *54* (27), 7905−7910.
(65) Li, D.; Wu, H.; Cheng, H.-C.; Wang, G.; Huang, Y.; Duan, X. Electronic and ionic transport dynamics in organolead halide perovskites. *ACS Nano* **2016**, *10* (7), 6933−6941.
(66) Zhao, Y.-C.; Zhou, W.-K.; Zhou, X.; Liu, K.-H.; Yu, D.-P.; Zhao, Q. Quantification of light-enhanced ionic transport in lead iodide perovskite thin films and its solar cell applications. *Light Sci. Appl.* **2017**, *6*, No. e16243.
(67) Harvey, S. P.; Li, Z.; Christians, J. A.; Zhu, K.; Luther, J. M.; Berry, J. J. Probing perovskite inhomogeneity beyond the surface: TOF-SIMS analysis of halide perovskite photovoltaic devices. *ACS Appl. Mater. Interfaces* **2018**, *10* (34), 28541−28552.
(68) Febriansyah, B.; Li, Y.; Giovanni, D.; Salim, T.; Hooper, T. J. N.; Sim, Y.; Ma, D.; Laxmi, S.; Lekina, Y.; Koh, T. M.; Shen, Z. X.; Pullarkat, S. A.; Sum, T. C.; Mhaisalkar, S. G.; Ager, J. W.; Mathews, N. Inorganic frameworks of low-dimensional perovskites dictate the performance and stability of mixed-dimensional perovskite solar cells. *Mater. Horiz.* **2023**, *10*, 536−546.
(69) Zhu, H.; Yang, W.; Reo, Y.; Zheng, G.; Bai, S.; Liu, A.; Noh, Y.-Y. Tin perovskite transistors and complementary circuits based on A-site cation engineering. *Nat. Electron.* **2023**, *6*, 650−657.
(70) Liu, A.; Zhu, H.; Bai, S.; Reo, Y.; Zou, T.; Kim, M.-G.; Noh, Y.-Y. High-performance inorganic metal halide perovskite transistors. *Nat. Electron.* **2022**, *5*, 78−83.
(71) Wang, Z.; Nayak, P. K.; Caraveo-Frescas, J. A.; Alshareef, H. N. Recent developments in p-type oxide semiconductor materials and devices. *Adv. Mater.* **2016**, *28* (20), 3831−3892.

https://doi.org/10.1021/acsami.4c17017
ACS Appl. Mater. Interfaces 2025, 17, 8501−8512